ARTICLE

A viscous switch for liquid-liquid dewetting

A.M.J. Edwards [1], R. Ledesma-Aguilar [2]*, M.I. Newton [1], C.V. Brown [1] & G. McHale [2]

The spontaneous dewetting of a liquid film from a solid surface occurs in many important processes, such as printing and microscale patterning. Experience suggests that dewetting occurs faster on surfaces of higher film repellency. Here, we show how, unexpectedly, a surrounding viscous phase can switch the overall dewetting speed so that films retract slower with increasing surface repellency. We present experiments and a hydrodynamic theory covering five decades of the viscosity ratio between the film and the surrounding phase. The timescale of dewetting is controlled by the geometry of the liquid-liquid interface close to the contact line and the viscosity ratio. At small viscosity ratio, dewetting is slower on low film-repellency surfaces due to a high dissipation at the edge of the receding film. This situation is reversed at high viscosity ratios, leading to a slower dewetting on high film-repellency surfaces due to the increased dissipation of the advancing surrounding phase.

[1] School of Science and Technology, Nottingham Trent University, Clifton Lane, Nottingham NG11 8NS, UK. [2] Smart Materials and Surfaces Laboratory, Department of Mathematics, Physics and Electrical Engineering, Northumbria University, Ellison Place, Newcastle upon Tyne NE1 8ST, UK. *email: rodrigo.ledesma@northumbria.ac.uk

The dewetting of a liquid–liquid film involves the motion of molecules at scales comparable with the thickness of the fluid–fluid interface. Greater understanding of the dynamics of the three-phase contact line can hence provide the valuable ability to predict and control the speed of a dewetting fluid film immersed in an ambient viscous liquid, which is important from both fundamental and applied perspectives. For instance, in oil recovery, forced imbibition is used to displace a more viscous phase from a porous material[1]. In the field of micropatterning, which is of wide relevance to produce sensors for biotechnology and microsystems, thin polymer films are used to drive the spontaneous formation of droplet patterns upon dewetting[2].

In a liquid–liquid system, spontaneous dewetting occurs when the surface energy of a solid covered by a thin liquid film (inner liquid) surrounded by an ambient liquid (outer liquid) is reduced upon removal of the film. In other words, a thin film will dewet from a flat solid whenever the spreading parameter, $S = \gamma_{so} - (\gamma + \gamma_{si})$, is negative, a situation controlled by the combination of the surface energies of the solid/outer liquid (γ_{so}), the solid/inner liquid (γ_{si}), and liquid–liquid (γ) interfaces[3]. If, in addition, gravitational effects are negligible, a situation that occurs for small liquid volumes or for density-matched liquids, the film will eventually form a spherical-cap-shaped droplet that intersects the solid with Young's angle θ_e, given by $\cos \theta_e = (\gamma_{so} - \gamma_{si})/\gamma$.

The excess surface energy per unit area of a liquid film before dewetting can be written as $\Delta E = \gamma(1 - \cos \theta_e)$. Therefore, the energy available to drive the dewetting process increases on surfaces that repel the film, i.e., those where θ_e is higher. Hence, one might expect that, all other things equal, dewetting will occur more quickly as the film repellency of the solid is increased, for instance, by increasing θ_e. Indeed, the first studies of dewetting reported a typical dewetting speed $U \propto \theta_e^3$[4], and subsequent experimental and theoretical studies of dewetting in the presence of a gas phase have either verified or assumed this result[5–12].

Here, we show an unexpected effect, where dewetting films switch their response to surfaces of low- and high-film repellency when an ambient liquid of sufficiently high viscosity is introduced. When the ratio of the viscosity of the outer liquid to the inner liquid is small, dewetting occurs faster on surfaces of increasing film repellency as previously reported[4]. However, for high viscosity ratios, the formation of a sharp wedge of outer fluid at high θ_e increases the viscous dissipation within the outer wedge, leading to longer dewetting times on surfaces of higher film repellency compared with surfaces of lower film repellency.

Results

We studied the dewetting of circular thin liquid films of trimethylolpropane triglycidyl ether (TMP-TG-E; mass density $\rho_i = 1166 \, \text{kg m}^{-3}$, dynamic viscosity $\mu_i = 189 \, \text{mPa s}^{-1}$) immersed in liquid polydimethylsiloxane hydroxyterminated of various viscosities (PDMS; mass density $\rho_o = 960 \, \text{kg m}^{-3}$, dynamic viscosity range $\mu_0 = 2 \, \text{mPa s}^{-1} - 104.85 \, \text{Pa s}^{-1}$). To create the liquid films, we used the physical principle of dielectrowetting reported by McHale et al.[13] and the experimental approach developed by Edwards et al.[12]. Solid substrates were patterned with a series of inter-digitated electrodes arranged to create a circular patch of radius $R_0 = 2.5 \, \text{mm}$. The electrodes were coated with a thin dielectric layer to form a smooth, flat surface, then treated with NOVEC 2702 or Teflon AF to create surfaces of different film repellency. The liquid–liquid surface tension is $\gamma = 6.2 \, \text{mN m}^{-1}$, giving a capillary length $l_c = \left[\gamma/(\rho_i - \rho_o)g\right]^{1/2} \approx 1.7 \, \text{mm}$. Hence, small TMP-TG-E droplets of volume $\Omega \approx 1 \, \mu\text{L}$ in ambient PDMS form equilibrium spherical-cap shapes of contact angle $\theta_e = 56° \pm 5°$ and $\theta_e = 137° \pm 8°$ on NOVEC and Teflon surfaces,

respectively (Fig. 1). Therefore, NOVEC has a low-film repellency compared with Teflon.

Once a droplet was deposited on the solid substrate, a voltage V was applied to the electrodes. This induces a nonuniform electric field of dielectrophoretic energy proportional to V^2[14,15]. The droplet responds by spreading over the solid until it covers an area such that the overall energy (surface plus dielectrophoretic) is minimized. Above a threshold voltage, $V_{th} \approx 300 \, \text{V}$, the liquid spreads completely over the solid patch above the electrodes to create a thin liquid film of circular footprint, whose average thickness, $h_0 \approx \Omega/\pi R_0^2 \approx 50 \, \mu\text{m}$, we estimate by assuming a cylindrical geometry (Fig. 1). To avoid entrainment of the outer PDMS oil under the TMP-TG-E film, which can lead to the formation of small entrapped droplets of the ambient fluid[16,17], the TMP-TG-E was spread to a thin film in air prior to immersion of the experimental device in the ambient bath of PDMS oil.

Removing the applied voltage introduces a sudden change in the free energy of the system, so the liquid film undergoes spontaneous dewetting from the solid driven purely by interfacial forces to recover the original spherical-cap droplet shape. Because the viscosity of PDMS can be varied over several decades, we were able to study the dewetting process on Teflon and NOVEC surfaces over five decades of the ratio of the viscosity of the outer to the inner liquid, $M = \mu_o/\mu_i$, with little change in the interfacial tension. During the dewetting process, the temperature was recorded to be $21 °C \pm 0.5 °C$, leading to negligible changes in the physical properties of both fluids (see the Methods section for a discussion of the effect of temperature on our measurements).

Figure 1 shows representative image sequences of experiments at the low and high extremes of viscosity ratio studied, i.e., $M = 0.01$ and $M = 555$ (see Supplementary Movie 1 for an example dewetting experiment). In all cases, the film eventually reaches a spherical-cap equilibrium shape. The overall dewetting time, however, is strongly dependent on the outer viscosity. On the low-film-repellency surface (NOVEC), the dewetting time increases approximately from 10 s to 270 s; while on the high-film-repellency surface (Teflon) the increase is much more pronounced: approximately from 500 ms to 1500 s.

While the overall increase in the dewetting time with increasing outer viscosity is intuitive, the observed dependence on the surface film repellency is not. From Fig. 1, one sees that, at low viscosity ratio, dewetting is faster—by a factor of 20—on the high-film-repellency surface (where θ_e is higher). This is consistent with previous experimental and theoretical studies of contact-line dynamics[18], where one expects that the interface speed increases with increasing θ_e. However, at high viscosity ratio this trend is reversed, and the liquid dewets about five times faster on the low-film-repellency surface.

Upon closer inspection of the images in Fig. 1, we note two distinct stages in the dewetting dynamics. After a short initial transient, the film forms a capillary rim, which grows in size by collecting liquid from the receding edge of the film (orange shading in Fig. 1a, b). Then, at a time $t = \tau_{rim}$, the rim merges at the center of the film, and the liquid relaxes to form a spherical-cap-shaped drop (blue shading in Fig. 1a, b). To characterize these regimes, let us define the reduced base radius, $R_x(t) = (R(t) - R_e)/(R_0 - R_e)$, where $R(t)$ is the instantaneous base radius of the liquid film and R_e is the final equilibrium base radius of the drop, shown in Fig. 1c. Regardless of the specific solid and liquid properties, the motion of the rim is always characterized by a linear decrease of $R_x(t)$, i.e., $U = dR/dt = \text{const}$. Henceforth, we refer to this as the linear regime. At low viscosity ratio, $U = 5.4 \, \text{mm s}^{-1}$ on Teflon, which is significantly larger compared with $U = 0.2 \, \text{mm s}^{-1}$ on Novec. However, at high viscosity ratio, U becomes comparable on both surfaces, regardless of the film repellency; $U = 0.02 \, \text{mm s}^{-1}$ and $0.01 \, \text{mm s}^{-1}$ on Teflon and Novec, respectively. The cross-over to
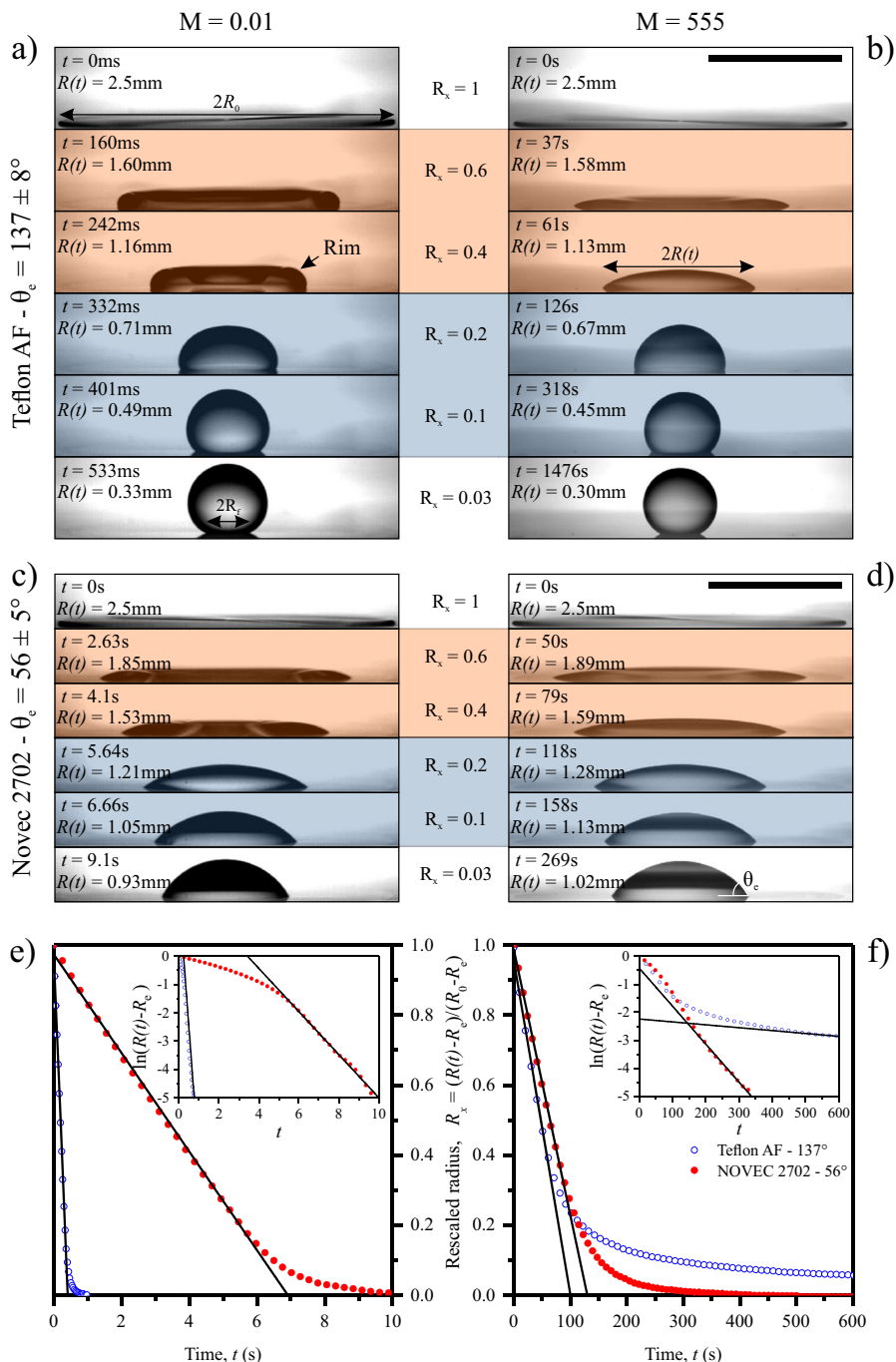
Fig. 1 Liquid–liquid film dewetting. a, b Time-sequence images of the dewetting of a trimethylolpropane triglycidyl ether (TMP-TG-E) film on a Teflon surface (high-film repellency) at viscosity ratio (**a**) $M = 0.01$ and (**b**) $M = 555$. **c, d** Time-sequence images of the dewetting of a TMP-TPG-E film on a NOVEC 2702 surface (low-film repellency) at (**c**) $M = 0.01$ and (**d**) $M = 555$. **e, f** Rescaled radius $R_x(t)$ vs time t for (**e**) $M = 0.01$ and (**f**) $M = 555$ for a single experiment on surfaces of different film repellency. The blue (empty) and red (full) symbols correspond to Teflon and NOVEC surfaces, respectively. The inset shows the exponential fitting to the data. The scale bars correspond to 2 mm.

the spherical-cap droplet shape (corresponding to $t > \tau_{rim}$) occurs for $R_x \approx 0.2$; from this point, $R(t)$ decreases exponentially to reach the final equilibrium radius, R_e. At low M, the relaxation timescale of this exponential regime is shorter on a surface of high-film repellency; however, at high M this trend is reversed, so the relaxation is now longer on that surface, despite a higher driving excess surface energy. Hence, the viscosity ratio between the film and the ambient liquid acts as a switch, controlling the relative timescale of dewetting on surfaces of different film repellency.

Comparing the images of the film at $M = 0.01$ and $M = 555$ in Fig. 1a (Teflon; high-film repellency), one sees that the shape of the rim is strongly affected by the viscosity of the outer liquid. For low M, the rim is strongly curved, and intersects the solid with an apparent contact angle $\theta \approx 90°$. On the other hand, for high M the curvature of the rim is much weaker, with an apparent contact angle $\theta \approx 30°$. A similar effect, although less pronounced, is observed for the thin liquid films dewetting on NOVEC (low-film repellency), where the contact angle of the

rim is reduced from $\theta \approx 25°$ to $\theta \approx 20°$ for low and high M, respectively.

The cross-sectional shape of the rim can be well approximated by a circular arc, suggesting that surface tension is able to smooth out the interface at scales comparable with the size of the rim. Close to the receding edge, however, we expect that the circular profile is distorted by the competition between the surface tension of the liquid–liquid interface and the viscous stresses arising from the flow pattern of the inner and outer liquids. As one approaches the contact line, the thickness of the rim is limited by the molecular size, ℓ. Here, the local orientation of the interface is no longer affected by hydrodynamic effects, and reaches a limiting contact angle, $\theta_m \approx \theta_e$. At large distances from the edge the hydrodynamic flows bend the interface, until this reaches the macroscopic apparent contact angle θ at a length scale $L \propto R_f \approx 1$ mm.

From wetting hydrodynamics, the bending of the interface profile in a planar surface geometry is governed by the Cox-Voinov relation[19],

$$\int_{\theta_e}^{\theta} \frac{d\theta'}{f(\theta', M)} = -\frac{\mu_i U}{\gamma} \ln\left(\frac{R_f}{\ell}\right), \quad (1)$$

where

$$f(\theta, M) = \frac{2\sin\theta\{M^2(\theta^2 - \sin^2\theta) + 2M((\pi - \theta)\theta + \sin^2\theta) + (\pi - \theta)^2 - \sin^2\theta\}}{M(\theta^2 - \sin^2\theta)(\pi - \theta + \sin\theta\cos\theta) + ((\pi - \theta)^2 - \sin^2\theta)(\theta - \sin\theta\cos\theta)}. \quad (2)$$

To maintain a circular shape, the speed of the inner edge of the rim, which connects to the thin film, must match the speed of the outer edge (see Fig. 2). Here, the bending of the interface is such that its inclination vanishes when the thickness of the rim reaches the film thickness, h_0. Hence, the Cox-Voinov relation reads

$$\int_{0}^{\theta} \frac{d\theta'}{f(\theta', M)} = \frac{\mu_i U}{\gamma} \ln\left(\frac{R_f}{h_0}\right). \quad (3)$$

Equations (1) and (3) can be combined to eliminate θ, yielding an expression of the speed of the interface as a function of the equilibrium angle and the viscosity ratio, i.e.,

$$U = \frac{\gamma}{\mu_i \ln(R_f^2/h_0\ell)} \int_{0}^{\theta_e} \frac{d\theta'}{f(\theta', M)}. \quad (4)$$

Figure 3a shows a comparison of this prediction of the rim speed with the experimental data, where we have used $\ell = 1$ nm and $\ell \sim 100$ nm[20] as the molecular sizes for NOVEC and Teflon, respectively. Overall, the theory predicts the experimental data well.

To illustrate the dependence of the speed of the interface with the viscosity ratio, let us consider the small-angle approximation, $\theta_e < 1$, and study the low- and high-M limits in Eq. (4). For small M, the bending of the interface is dominated by the viscous flow within the film. Letting $M \ll 1$ leads to $f(\theta, M) \to 3/\theta^2 + 9M/2\pi\theta$. The resulting rim speed, $U \approx \gamma\theta_e^3(1 - 27\theta_e M/8\pi)/9\mu_i\ln(R_f^2/h_0\ell)$, has a leading-order term controlled by a strong (power-law) dependence on the equilibrium contact angle. The viscosity ratio enters as a correction, which reduces the speed at a rate that increases with θ_e (hence explaining the stronger variation of $U(M)$ measured on a high-repellency (Teflon) surface. On the other hand, by letting $M \gg 1$, we find the asymptotic behavior $f(\theta, M) \to 2M\theta/\pi$, which leads to $U \approx \gamma\pi \ln\theta_e/2\mu_o\ln(R_f^2/h_0\ell)$. Hence, the interface profile is dominated by the flow of the outer liquid, up to a weak (logarithmic) dependence on the equilibrium contact angle, which explains why at high viscosity ratio the dewetting
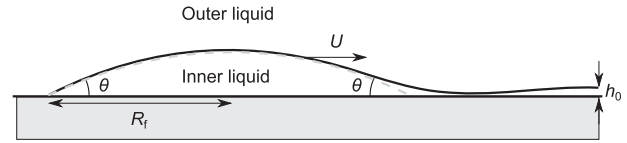

Fig. 2 Schematic representation of a dewetting rim. The interface profile is approximated by a circular arc of base radius R_f and apparent contact angle θ at the receding and the advancing edges. The rim connects to a film of typical thickness h_0. The rim recedes at a speed U.
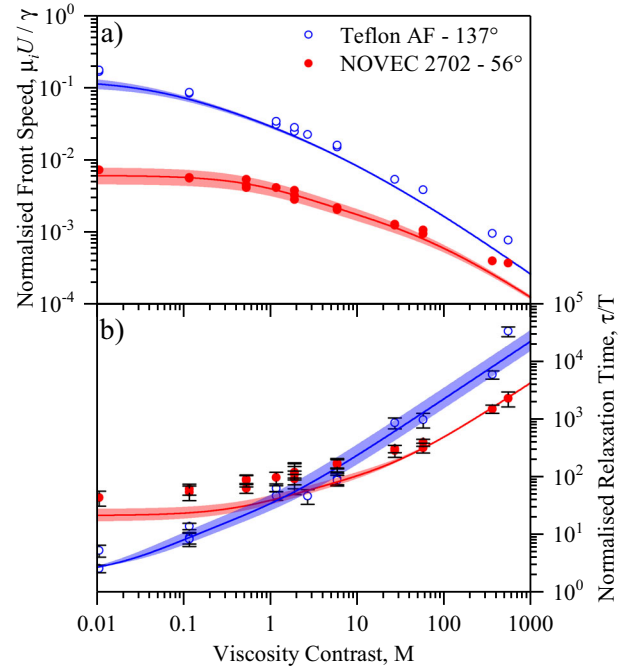

Fig. 3 Linear and exponential dewetting regimes. a Speed of the dewetting front, U, vs viscosity ratio, M, during the linear dewetting regime of the thin film. The speed is normalized using the characteristic speed γ/μ_i, where γ is the interfacial tension and μ_i is the viscosity of the (inner) dewetting liquid. **b** Exponential time constant, τ, vs viscosity ratio, M, during the exponential relaxation of the droplet towards equilibrium. The relaxation time is normalized using the characteristic time $T = \mu_i\Omega^{1/3}/\gamma$, where Ω is the droplet volume. The blue (empty) and red (full) symbols correspond to experimental results on Teflon and NOVEC surfaces, respectively. The solid lines correspond to the theoretical prediction of Eqs. (4) and (8), using an inner fluid viscosity $\mu_i = 189$ mPa s^{-1}, interfacial tension $\gamma = 6.2$ mN m^{-1}, rim radius $R_f = 1$ mm, and film thickness $h_0 = 50$ μm, all set using the experimentally measured values. The light-colored bands correspond to the uncertainty in the theoretical prediction due to the uncertainty in the equilibrium contact angle. Error bars for M and $\mu_i U/\gamma$ are smaller than the symbols; error bars for τ/T correspond to the uncertainty in the fit to an exponential of the data of the instantaneous base radius of the dewetting liquid, R, vs time, t.

speed on surfaces of very different film repellency becomes comparable.

Our experimental measurements of the relaxation time, τ, which are extracted from exponential fits of the $R(t)$ data (see insets in Fig. 1c), reveal a cross-over to a slower relaxation on the Teflon surface at $M \approx 1$ [see Fig. 3b]. As the capillary rim merges and the droplet base radius approaches R_e, the droplet morphology is well described by a smooth succession of spherical-cap shapes (Fig. 1, $R_x < 0.2$); hence the base radius of

the droplet and the apparent contact angle are related by geometry, i.e.,

$$R(\theta) = \left[\frac{3\Omega}{\pi\beta(\theta)}\right]^{1/3}, \qquad (5)$$

where $\beta(\theta) = (1 - \cos\theta)^2 (2 + \cos\theta)/\sin^3\theta$. As $\theta \rightarrow \theta_e$, the excess contact angle, $\Delta\theta = \theta_e - \theta$, vanishes, and Eq. (5) can be expressed in differential form as

$$dR = h(\theta_e) R_e d\Delta\theta, \qquad (6)$$

where $h(\theta_e) = \tan(\theta_e/2)/(2 - \cos\theta_e - \cos^2\theta_e)$. To couple this geometrical relation to the dynamics of the droplet's edge, we use the Cox–Voinov relation, i.e.,

$$\Delta\theta = f(\theta_e, M)\frac{\gamma U}{\mu_i}\ln\left(\frac{R_e}{\ell}\right), \qquad (7)$$

where we have taken the approximation $\int_{\theta_e}^{\theta_e - \Delta\theta} d\theta'/f(\theta', M) \approx -\Delta\theta/f(\theta_e, M)$.

Combining Eqs. (6) and (7) gives the exponential decay $\Delta\theta = \tau d(\Delta\theta)/dt$, where the relaxation time obeys

$$\tau = \frac{\mu_i R_e}{\gamma}\ln\left(\frac{R_e}{\ell}\right)f(\theta_e, M)h(\theta_e), \qquad (8)$$

which can be expressed in dimensionless form by defining the characteristic time $T \equiv \mu_i\Omega^{1/3}/\gamma$. Figure 3b shows a comparison of the experimental measurement of the relaxation time with the prediction of Eq. (8). The experimental error bars correspond to the fitting error to the expected exponential dependence. The uncertainty bands of the theoretical prediction are due to the uncertainty in the equilibrium contact angle, θ_e. Overall, the theoretical prediction is in good agreement with our experimental measurements of the relaxation time, and captures the observed cross-over of τ on surfaces of low- and high-film repellency at large M. The low-M behavior of the relaxation time is $\tau \approx (\mu_i/\gamma)\ln(R_e/\ell)\left[4\Omega/\pi\theta_e^{10}\right]^{1/3}(1 + 3M\theta_e/2\pi)$, which, again, has a power-law dependence on the equilibrium contact angle, and increases with the viscosity ratio. However, as shown in Fig. 3b, τ increases at a much higher rate with increasing θ_e. This is because the geometry of the outer liquid close to the contact line corresponds to an acute wedge of contact angle $\approx \pi - \theta_e$, which leads to a higher dissipation at large θ_e. At high M, this effect dominates the dynamics, giving a longer relaxation time with increasing film repellency. Overall, the cross-over of the relaxation time occurs gradually, and hence it is not characterized by a typical value of the viscosity ratio.

To summarize, we have reported the dewetting of thin circular liquid films immersed in an ambient viscous phase over five decades of viscosity ratio, demonstrating the existence of an unexpected viscous switch effect that controls the timescale of dewetting. The switch effect is a consequence of the interplay between the excess energy due to the surface energy, which drives the dewetting process, and the dissipation due to the geometry of the fluid flow, which resists it. Finally, our work brings the commonly accepted concept of "fast" motion of a liquid on a liquid-repellent surface into question, and opens up the possibility of identifying similar switch effects in other situations involving dynamic wetting where the role of an ambient viscous phase remains to be understood. These include the dewetting of oil droplets from solid fibers in detergency, the forced imbibition of the viscous phase in oil recovery[1], and the motion of immersed droplets on surfaces of variable wettability in microfluidics[21].

Methods

Electrode manufacture. IDE's were produced using a lift-off photolithographic method with a titanium–gold–titanium metallic layer. Glass slides (37.5 mm ×

25 mm) were first cleaned using 5, 0.5, and 0% solutions of Decon 90 (Decon Laboratories) mixed with deionized (DI) water ultrasonicated for 480 s and thoroughly rinsed with DI water between steps. Cleaned substrates were then soaked in 2-propanol (Fisher Scientific) and then dried under nitrogen flux. A 1.5 -μm layer of S1813 G2 photoresist (Dow) was then spin-coated on to the substrates before soft baking at 110 °C for 75 s. The photoresist layer was then UV exposed using a SUSS MBJ4 mask aligner for 1 s through the 5 mm diameter, 20 μm linewidth/gap concentric circle electrode pattern. Exposed substrates were then developed using Microposit developer concentrate (Dow) mixed in a 50:50 solution with DI water, this development revealed a negative of the final structure. Negatives were then metallized with a titanium–gold–titanium sandwich structure of thickness 10–20–10 nm using a K575X sputter coater (Emitech). Remaining photoresist was then stripped using Acetone (Fisher Scientific). IDE's were then cleaned again and coated with a 100 -nm thick layer of Omnicoat (Dow) to act as an adhesion layer for the 1 -μm SU8-2 (Dow) dielectric layer, which prevents electrical conduction through the liquids.

Electrical addressing and surface treatment. The electrical addressing to the IDE's was performed by an Agilent 33500B waveform generator providing a 10 KHz sine wave to a PZD700A (Trek Inc.) amplifier, which multiplies the input signal 100 ×. The uniformity of the output waveform was measured using an DSO6014A (Agilent) oscilloscope, and the applied voltage was monitored using a 34410 A (Agilent) digital voltmeter. To promote retraction of the TMP-TG-E in the PDMS, substrates were coated with two separate oleophobic materials, Teflon AF mixed in a 0.5% by weight solution with its solvent, and the commercially available NOVEC 2702, electronic grade coating (3 M). Substrates were dip-coated in both solutions allowed to dry at room temperature before baking at 155 °C for 20 min to cure. The surface roughness of the coated samples was measured using an Veeco Dektak 6 M surface profilometer across the active electrode areas. The measurements show that, at small scales, the surfaces on the small scale have an arithmetic mean deviation surface roughness of 39.5 ± 0.8 nm for the NOVEC 2702 surface and 26 ± 9 nm for the Teflon AF surface. At larger scales, the measurements show surface features arising from the drying of the surface coatings, which may act to momentarily pin the contact line. We expect these features to contribute to the small-scale noise in the measurement of the contact-line motion, which becomes dominant at the end of the relaxation of the droplets. For this reason, we make the measurement of the relaxation time in a window above this limit within the range $0.01 < R(t) - R_e < 0.2$.

Image capture and analysis. Images were captured from both the side and top of the droplet, depending on the timescale of retraction framerates for both cameras were set appropriately. Top images were captured using an EO-13122C (Edmund Optics) fitted with a ×4 objective up to 150 FPS. Side images were captured using an HHC x4 camera (Mega Speed Corporation) fitted with a ×5 objective lens up to 1500 FPS. The contact angle and base radius of the droplet were determined by a developed MatLAB program with a user determined baseline. Apparent contact angle was calculated by fitting a tangent to Np points above the baseline, this tangent was then extrapolated to find the apparent contact angle at the solid substrate. As the refractive index difference between the two liquids is 0.07 to improve contrast the TMP-TG-E was dyed using Sudan Orange II (CAS number: 3118-97-6) at a concentration of 0.1% by wt.

Data fitting. The fitting procedure for the relaxation time, τ, is as follows. We first plot a graph of $\ln(R(t) - R_e)$ vs t, where R_e is taken as the final measured value of the droplet base radius. We then fit a set of straight lines to the data in the range $0.01 < R(t) - R_e < 0.2$. We then vary R_e and look for a maximum value of the linear regression coefficient (R^2). To compute the uncertainty in the relaxation time due to an uncertainty in the base radius, we set an error margin δR_e and compute the corresponding margin $\delta\tau$ based on the linear regression.

Materials characterization. We characterized the density, viscosity, and interfacial tension between the two fluids using the following techniques. Density measurements were made using an Anton Parr DMA 4500 density meter over the range 10 °C to 25 °C for TMP-TG-E finding a variation of the mass density of 0.00043 g cm^{-3} per 0.5 °C. The density of PDMS oils was obtained from the manufacturer (Alfa Aesar), and the influence of temperature on the density was obtained from Roberts et al.[22]. The viscosity of all liquids used in the experiments was measured using a TA Instruments CSL^2 100 rheometer across the temperature range 20 °C to 22 °C. We measured the interfacial tension between TMP-TG-E and PDMS using the pendant droplet method with a Krüss DSA 10-MK2 equipment at a temperature of 20 °C. We took 40 separate measurements of the interfacial tension for two different viscosity grades of PDMS finding that the interfacial tension does not vary significantly with oil viscosity. The average measured value of the interfacial tension is $\gamma = 6.2 \pm 0.3$ mN m^{-1}.

References
1. Trojer, M., Szulczewski, M. L. & Juanes, R. Stabilizing fluid-fluid displacements in porous media through wettability alteration. *Phys. Rev. Appl.* **3**, 054008 (2015).
2. Telford, A. M., Thickett, S. C. & Neto, C. Functional patterned coatings by thin polymer film dewetting. *J. Colloid Interface Sci.* **507**, 453–469 (2017).
3. de Gennes, P. G. Wetting: statics and dynamics. *Rev. Mod. Phys.* **57**, 827–863 (1985).
4. Redon, C., Brochard-Wyart, F. & Rondelez, F. Dynamics of dewetting. *Phys. Rev. Lett.* **66**, 715–718 (1991).
5. Andrieu, C., Sykes, C. & Brochard, F. Dynamics of fast dewetting on model solid substrates. *J. Adhes.* **58**, 15–24 (1996).
6. Shull, K. R. & Karis, T. E. Dewetting dynamics for large equilibrium contact angles. *Langmuir* **10**, 334–339 (1994).
7. Haidara, H., Vonna, L. & Schultz, J. Instability and dewetting of confined thin liquid films in nonmiscible external bulk fluids (water and aqueous surfactant solutions): experiments versus theoretical predictions. *Langmuir* **14**, 3425–3434 (1998).
8. de Gennes, P. G., Brochard-Wyart, F. & Quéré, D. *Capillary and Wetting Phenomena: Drops, Bubbles, Pearls, Waves* (Springer Science & Business Media, New York, 2004).
9. Fetzer, R., Jacobs, K., Münch, A., Wagner, B. & Witelski, T. P. New slip regimes and the shape of dewetting thin liquid films. *Phys. Rev. Lett.* **95**, 127801 (2005).
10. Snoeijer, J. H. & Eggers, J. Asymptotic analysis of the dewetting rim. *Phys. Rev. E* **82**, 056314 (2010).
11. McGraw, J. D. et al. Slip-mediated dewetting of polymer microdroplets. *Proc. Natl Acad. Sci. USA* **113**, 1168–1173 (2016).
12. Edwards, A. M. J., Ledesma-Aguilar, R., Newton, M. I., Brown, C. V. & McHale, G. Not spreading in reverse: the dewetting of a liquid film into a single drop. *Sci. Adv.* **2**, e1600183 (2016).
13. McHale, G., Brown, C. V., Newton, M. I., Wells, G. G. & Sampara, N. Dielectrowetting driven spreading of droplets. *Phys. Rev. Lett.* **107**, 186101 (2011).
14. Brown, C. V., Wells, G. G., Newton, M. I. & McHale, G. *Nat. Photo* **3**, 403 (2009).
15. Edwards, A. M. J., Brown, C. V., Newton, M. I. & McHale, G. Dielectrowetting: the past, present, and future. *Curr. Opin. Colloid Interface Sci.* **36**, 28–36 (2018).
16. Staicu, A. & Mugele, F. Electrowetting-induced oil film entrapment and instability. *Phys. Rev. Lett.* **97**, 167801 (2006).
17. Baratian, D., Ruiz-Gutiérrez, É., Mugele, F. & Ledesma-Aguilar, R. Slippery when wet: mobility regimes of confined drops in electrowetting. *Soft Matter* **15**, 7063–7070 (2019).
18. Bonn, D., Eggers, J., Indekeu, J., Meunier, J. & Rolley, E. Wetting and Spreading. *Rev. Mod. Phys.* **81**, 739–805 (2009).
19. Cox, R. G. The dynamics of the spreading of liquids on a solid surface. Part 1. Viscous flow. *J. Fluid Mech.* **168**, 169–194 (1986).
20. Othmer, K. *Encyclopedia of Chemical Technology*. 5th Edn (Wiley-Blackwell, USA, 2007).
21. 't Mannetje, D. et al. Trapping of drops by wetting defects. *Nat. Commun.* **5**, 3559 (2014).
22. Roberts, C. et al. *Sandia Report SAND2017-1242* (Sandia National Laboratories, 2017).

Author contributions
A.M.J.E., C.V.B., M.I.N. and G.M. designed the experiments. A.M.J.E. carried out the experiments. A.M.J.E., R.L.-A. and C.V.B. analyzed the data. R.L.-A. and G.M. developed the theoretical model. All authors contributed to writing the paper.

Competing interests
The authors declare no competing interests.

Additional information
Supplementary information is available for this paper at https://doi.org/10.1038/s42005-020-0284-8.

Correspondence and requests for materials should be addressed to R.L.-A.

Reprints and permission information is available at http://www.nature.com/reprints

Publisher's note Springer Nature remains neutral with regard to jurisdictional claims in published maps and institutional affiliations.